Emission characteristics of greenhouse gases and air pollutants in a Qinghai-Tibetan Plateau city using a portable Fourier transform spectrometer and TROPOMI observations

Qiansi Tu[1], Frank Hase[2], Ying Zhang[3], Jiaxin Fang[1], Yanwu Jiang[1], Xiaofan Li[3], Matthias Schneider[2], Zhuolin Yang[3], Xin Zhang[4], Zhengqiang Li[3]

[1]School of Mechanical Engineering, Tongji University, Shanghai 201804, China
[2]Institute of Meteorology and Climate Research (IMK-ASF), Karlsruhe Institute of Technology (KIT), Eggenstein-Leopoldshafen 76344, Germany
[3]State Environmental Protection Key Laboratory of Satellite Remote Sensing, Aerospace Information Research Institute, Chinese Academy of Sciences, Beijing 100101, China
[4]College of Resources and Environment, University of Chinese Academy of Sciences, Beijing 101408, China

Correspondence to: Zhengqiang Li (lizq@radi.ac.cn)

Abstract

Despite the critical need to understand greenhouse gas and air pollutant concentrations and their emissions characteristics in urban and industrial areas, limited assessments have been conducted in the Qinghai-Tibetan Plateau (QTP) cities. Herein, for the first time, we present CO_2, CH_4 and CO column abundances using a portal Fourier-transform infrared spectrometer (EM27/SUN) in Ganhe Industrial Park (36.546°N, 101.518°E, 2603 m a.s.l.), located in the suburbs of Xining, Qinghai Province, during May – June 2024. Ground-based measurements found to be higher than spaceborne measurements (TROPOMI and IASI) and model forecast (CAMS) across all investigated species, indicating higher local emissions. Notably, significant discrepancies in CO levels are observed, particularly under easterly wind conditions, which transport polluted airmasses from Xining city. To further quantify emissions, we applied a simple dispersion model to the EM27/SUN data and TROPOMI products, estimating an average CO emission rate of 12.3 ± 9.6 kg/s and 8.9 ± 7.5 kg/s, respectively. A wind-assigned anomaly method further applied to the TROPOMI dataset yielded a CO emission rate of 8.5 kg/s. Additionally, the ground-based observations of $\Delta XCO/\Delta XCO_2$ ratio exhibits a strong correlation under easterly winds, which suggests an average CO_2 emission rate of 550 kg/s from Xining city. These findings underscore the utility of portable FTIR spectrometers to enhance our understanding of urban emissions at QTP and demonstrate the potential of combining collaborative ground-based and spaced-based observations to estimate CO_2 emissions, particularly in regions with sparse CO_2 measurement coverage.

1. Introduction

Carbon dioxide (CO_2) and methane (CH_4) are two primary greenhouse gases (GHGs) whose atmospheric concentrations have surged to unprecedented levels since 1750, largely driven by anthropogenic activities. According to the WMO's annual Greenhouse Gas Bulletin (https://library.wmo.int/idurl/4/69057, last access: January, 2024), the globally averaged surface concentration of CO_2 reached 420 parts per million (ppm), and CH_4 reached 1934 parts per billion (ppb) in 2023. Carbon monoxide (CO) is one of the most important atmospheric pollutants, which is primarily produced by inefficient combustion, such as biomass burning (Griffin et al., 2024), traffic and industrial activity (Dils

36 et al., 2011). CO plays a crucial role in atmospheric chemistry, especially in the troposphere, where it reacts with the

37 hydroxyl radical (OH) in the reaction $CO + \cdot OH \rightarrow CO_2 + \cdot H$ (Spivakovsky et al., 2000; Thompson, 1992). This

38 oxidation process serves as the dominant sink for atmospheric CO, accounting for 90-95% of its total removal.

39 Consequently, CO indirectly affects the lifetime of CH_4 by reducing the availability of OH that would otherwise

40 oxidize CH_4. This, in turn, indirectly contributes to global warming (IPCC, 2007).

41 To achieve highly accurate and precise measurements of total column abundances of CO_2, CH_4 and CO, the Total

42 Carbon Column Observing Network (TCCON) and the Collaborative Carbon Column Observing Network (COCCON)

43 have been established. Both networks utilize Fourier-transform infrared (FTIR) spectrometers. TCCON employs high-

44 resolution FTIR instruments for exceptionally precise CO_2, CH_4 and CO measurements amongst other gases (Wunch

45 et al., 2011). In contrast, COCCON employs portable, low-resolution FTIR spectrometers to measure CO_2, CH_4 and

46 CO, providing a valuable complementary extension to the TCCON network (Alberti et al., 2022; Frey et al., 2015;

47 Herkommer et al., 2024).

48 The Qinghai-Tibetan Plateau (QTP), with its unique topography, plays a crucial role in Earth's climate system and

49 has become a key region for monitoring climate trends and global air quality (Kang et al., 2021; Zhang et al., 2022).

50 A recent study highlights that surface pollutants in Asia can be transported into the stratosphere from the Tibetan

51 Plateau region, potentially exerting significant impacts on global climate (Bian et al., 2020). There are only two

52 stations on the Tibetan Plateau—Waliguan, the only global station in Eurasia, and Shangri-La—that measure surface

53 concentrations of CO_2, CH_4, and CO, making them important for understanding atmospheric composition in this

54 critical region (Guo et al., 2020; Xiong et al., 2022). These stations conduct in-situ measurements and provide highly

55 accurate surface observations and valuable insights into local fluxes; however, they are influenced by surface

56 exchanges and vertical transport, which can limit their ability to estimate sources and sinks over larger spatial scales.

57 When combined with other observation types, such as FTIR, which capture emissions and transport on a broader scale,

58 they become complementary, together offering a more comprehensive understanding of sources and sinks at both local

59 and regional levels (Callewaert et al., 2022). Additionally, surface observations are less effective for satellite validation

60 compared to column-based measurements, such as those obtained from TCCON and COCCON. However, there are

61 currently no TCCON or COCCON stations on the QTP. Zhou et al. (2023) conducted the first FTIR column

62 observations in a small city on QTP, but measurements in larger cities, such as Xining—the capital of Qinghai

63 Province, remain sparse. This is notable since most anthropogenic emissions of GHGs and CO are concentrated in

64 urban centers (Crippa et al., 2021).

65 To quantify total emissions from the Xining area, we deployed an EM27/SUN FTIR spectrometer in Ganhe Industrial

66 Park (36.546°N, 101.518°E, 2603 m a.s.l.) during May-June 2024. The site was strategically positioned in the

67 southwest suburbs to capture integrated urban plumes downwind of the city center under prevailing easterly winds.

68 The early summer measurement period minimizes contributions from seasonal heating emissions—particularly

69 significant CO sources from combustion during colder months—thereby focusing on emissions more characteristic of

70 persistent urban sources. These ground-based measurements are complemented by co-located TROPOMI and IASI

71 satellite observations and CAMS model forecasts. Furthermore, we apply a simple dispersion model to estimate CO

72 and CO_2 emission rates from the urban area.

2. Methods and materials

2.1 Site description

75 A three-week field campaign was conducted in Ganhe Industrial Park (36.546°N, 101.518°E, 2603 m a.s.l.) from May

76 23 to June 14, 2024. The industrial park is located southwest of Xining, the capital of Qinghai Province, China (Figure

77 1) and was established in 2002 in the Huangzhong District. Xining, situated on the eastern edge of the Tibetan Plateau

78 and upstream of the Huangshui River, experiences a plateau mountain climate. In 2020, the city has a resident

79 population of approximately 2.47 million, with a density of 324 persons/km^2 (Xining Statistical Bureau, 2021), making

80 it the most densely populated area in Qinghai Province with nearly 80% of its population living in the urban center.
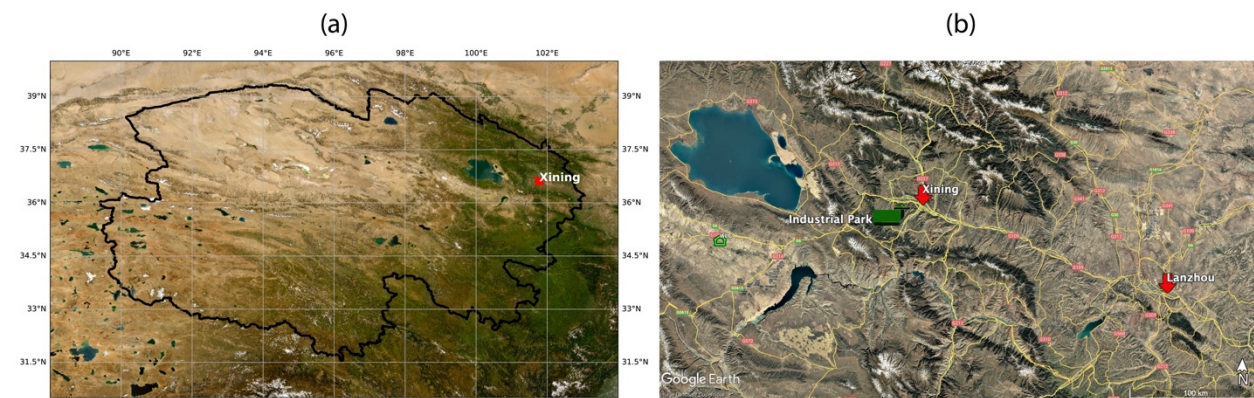
Figure 1: A terrain map showing Qinghai Province and the location of its capital city of Xining (Terrain information originates from World Imagery). A map illustrating the locations of the EM27/SUN instrument within the Ganhe Industrial Park, Xining city (Qinghai province), Lanzhou city (Gansu province), and Waliguan station. The base map is sourced from © Google Earth, Image © 2024 Maxar Technologies; Image © 2024 CNES / Airbus.

2.2 COCCON GHG products

87 In this study, a portable ground-based Fourier-transform infrared (FTIR) spectrometer, the EM27/SUN, was used.

88 Developed by the Karlsruhe Institute of Technology (KIT) in collaboration with Bruker Optics GmbH, Ettlingen,

89 Germany, the EM27/SUN is designed to measure solar absorption spectra in the near-infrared spectral range (covering

90 5500–11,000 cm^{-1} and 4000–5500 cm^{-1}) with a spectral resolution of 0.5 cm^{-1} (Gisi et al., 2012). The spectrometer

91 records double-sided, DC-coupled interferograms using two indium gallium arsenide (InGaAs) detectors at room

92 temperature (Hase et al., 2016). These interferograms are processed using a preprocessing tool and the PROFFAST

93 nonlinear least squares fitting algorithm, which was developed by KIT in the framework of the COCCON-

94 PROCEEDS project funded by the European Space Agency (ESA) (Alberti et al., 2022; Herkommer et al., 2024).

95 This approach enables the retrieval of atmospheric concentrations of trace gases such as O_2, CO_2, CH_4, CO and H_2O.

96 The gas column is then converted to column-averaged dry-air mole fractions of the gas (Xgas) by dividing the gas

97 column by the co-observed O_2 column, using the well-known mole fraction of O_2 in dry air.

98 With meanwhile about 200 EM27/SUN instruments deployed worldwide, these spectrometers are widely used for
99 monitoring GHG concentrations and air pollutant, for estimating emissions from various sources, and for validating
100 satellite measurements (Chen et al., 2020; Frey et al., 2015; Hase et al., 2015; Herkommer et al., 2024; Luther et al.,
101 2019; Tu et al., 2021, 2020). Due to its excellent level of robustness and reliability, the EM27/SUN instrument can be
102 applied in both field campaigns and long-term deployment at fixed sites. These observations complement TCCON at
103 various locations enhances global GHG monitoring efforts. In this context, the COCCON was established to further
104 advance and standardize these observational efforts.

105 The specific EM27/SUN instrument used in this campaign operates within the framework of COCCON. Prior to
106 deployment, the spectrometer was calibrated against the TCCON reference instrument at KIT to establish instrument-
107 specific calibration factors for each target gas, ensuring consistency with the TCCON data products (Frey et al., 2019).
108 To guarantee data quality and monitor instrumental stability throughout the campaign, a comprehensive quality control
109 (QC) and quality assurance (QA) protocol was implemented, following established COCCON procedures. This
110 protocol focuses on two key parameters: the Instrumental Line Shape (ILS) and the XAIR ratio. The ILS,
111 characterizing the spectrometer's spectral response function, was determined through laboratory measurements using
112 a nonlinear least-squares fitting algorithm (Frey et al., 2015; Hase et al., 1999). An ILS measurement performed in
113 December 2024 revealed a minor change (a ~1.5% decrease in modulation efficiency (ME)) compared to the pre-
114 campaign baseline at KIT, which is within the accepted uncertainty range and attributable to transportation. This small
115 change is attributed primarily to mechanical stresses incurred during the long-distance shipment from Germany to
116 China and subsequent domestic transports. A potential minor contribution from systematic errors associated with the
117 specific light source and lens used in the Chinese ILS setup cannot be entirely ruled out. The stability of the ILS was
118 confirmed by a subsequent measurement in September 2025 as no change was found in the ME value.

119 The XAIR ratio, derived from the measured vertical columns of O_2 and H_2O alongside surface pressure, served as an
120 independent indicator of instrumental performance. The mean XAIR value during the campaign was 1.0012 ± 0.0024,
121 with nearly identical values recorded before (1.0005) and after (1.0005) the measurement period, demonstrating
122 excellent instrumental stability. Furthermore, to minimize uncertainties related to air mass dependence, a strict solar
123 zenith angle (SZA) filter of <60º was applied to the data. The combination of rigorous calibration with respect to
124 TCCON, continuous stability monitoring via ILS and XAIR, and careful data filtering ensures the high quality and
125 reliability of the ground-based data, providing a solid foundation for the subsequent satellite validation exercise.

126 **2.3 TROPOMI CH_4 and CO products**

127 The TROPOspheric Monitoring Instrument (TROPOMI), single payload of the Sentinel-5 Precursor (S5P) satellite,
128 has been in orbit since October 2017. It operates in a low Earth polar orbit with a planned operational lifespan of 7
129 years. S5P is the first Copernicus mission and is designed to deliver daily global information on concentrations of
130 traces gases (e.g., CH_4 and CO) and aerosols, aiming to monitor air quality, climate forcing and ozone abundances
131 with high spatial and temporal resolution (Veefkind et al., 2012).

132 TROPOMI, currently the most advanced nadir-viewing and multispectral imaging spectrometer, was developed jointly
133 by the European Space Agency (ESA) and the Netherlands Space Office. It measures across several spectral bands:
134 ultraviolet (UV) and visible (VIS) (270–500 nm), near-infrared (NIR, 675–775 nm) and shortwave infrared (SWIR,
135 2305–2385 nm). With a wide swatch of 2600 km across track, TROPOMI provides operational level 2 (L2) CH_4 and
136 CO products with a very high spatial resolution of approximately 5.5 km × 7 km since August 2019.

137 The retrieval of TROPOMI total column abundances of CH_4 is conducted using the RemoTec-S5P algorithm (Butz et
138 al., 2009; Hasekamp and Butz, 2008). For CO, the total column retrieval is performed by a modified SWIR CO
139 retrieval (SICOR) algorithm, which is based on the CO absorption band between 2305 nm and 2385 nm, with
140 interfering trace gases and effective cloud parameters (Landgraf et al., 2016).

141 In this study, the TROPOMI L2 CH_4 and CO data with quality assurance values (qa_value) greater than 0.5, as
142 recommend in the S5P product readme files, are utilized. Detailed documentation can be accessed for the CH_4
143 (https://sentinel.esa.int/documents/247904/3541451/Sentinel-5P-Methane-ProductReadme-File, last accessed: June
144 9, 2025) and CO data products (https://sentinel.esa.int/documents/247904/3541451/Sentinel-5P-CarbonMonoxide-
145 Level-2-Product-Readme-File, last accessed: June 9, 2025).

2.4 IASI CO products

147 The Infrared Atmospheric Sounding Interferometer (IASI) is the primary payload carried on the EUMETSAT's
148 MetOp series of polar-orbiting satellites and delivers meteorological parameters (e.g., water vapour and atmospheric
149 temperature), and trace species with an unprecedented spatial and temporal coverage (Clerbaux et al., 2009). IASI
150 sensors are nadir looking thermal infrared sensors and there are currently three instruments in operation, which were
151 launched in 2006, 2012 and 2018.

152 The IASI CO dataset is processed using the Fast Optimal Retrievals on Layers for IASI (FORLI) software (George et
153 al., 2009; Hurtmans et al., 2012). The retrievals are performed within the 2143-2181.25 cm^{-1} spectral range based on
154 the optimal estimation theory and tabulated absorption cross sections at various pressures and temperatures to enhance
155 the efficiency of the radiative transfer calculation. The instrument provides global coverage with a 2200 km swath and
156 a 12 km resolution at nadir (George et al., 2009). In this study, total column abundances of CO from IASI onboard
157 Metop-C Level 2 (version 6.7) are used.

2.5 CAMS CAMS high-resolution GHG forecasts and CAMS-GLOB-ANT inventory

159 The Copernicus Atmosphere Monitoring Service (CAMS), which is implemented by the European Centre for
160 Medium-Range Weather Forecasts (ECMWF), produces daily global forecasts for the two main long-lived GHGs. As
161 part of the CAMS GHG services, the ECMWF Integrated Forecasting System (IFS) delivers 5-day high-resolution
162 forecasts of CO_2, CH_4 (Agustí-Panareda et al., 2014, 2017, 2019), as well as CO and meteorological parameters
163 essential for GHG forecasting (Flemming et al., 2015). The forecast is generated a few hours behind real time, with
164 initial conditions derived from a 4-day forecast of the analysis experiment. It is run at a horizontal resolution TCo1279,
165 corresponding to a cubic octahedral reduced Gaussian grid with an approximately spatial resolution of 9 km (Holm et

166 al., 2016). The model includes 137 vertical levels extending from the surface to 0.01 hPa (Agustí-Panareda et al.,
167 2019).

168 In this study, the forecasting suite is based on the IFS model cycle CY48R1, which was upgraded in June 2023. This
169 update introduced several system enhancements, particularly in composition modelling, emissions and assimilation
170 (Eskes et al., 2024). Notably, CY48R1 includes the assimilation of TROPOMI CO and the performance has generally
171 improved compared to all observations, such as surface observations, vertical profiles from IAGOS aircraft and
172 NDACC FTIR measurements, and satellite total column retrievals (Eskes et al., 2024).

173 CAMS also delivers global anthropogenic emissions, referred to as CAMS-GLOB-ANT. This includes emissions of
174 both air pollutants (e.g., CO) and greenhouse gases (e.g., CO_2 and CH_4) for real-time forecasts (Soulie et al., 2024).
175 Emissions are provided for 17 sectors and 35 species as monthly averages, with a spatial resolution of 0.1° × 0.1°,
176 covering the period from 2000 to 2025. This study uses the latest version v6.2, which is based on the Emissions
177 Database for Global Atmospheric Research (EDGARv6) and employs the same methodology as v5.3.

178 **2.6 Dispersion model and wind-assigned anomaly method**

179 For a single point source, the total emission is calculated by multiplying the measured total column enhancement (ΔCO)
180 by the area of the affected plume (Babenhauserheide et al., 2020). This plume area is modeled as an evenly distributed
181 cone, representing the long-term averaged dispersion (Tu et al., 2022a). The relationship is given by the following
182 equation:

$$\varepsilon = \Delta \text{CO} \times d \times v \times \partial \qquad \textbf{Eq. 1}$$

183 where ΔCO represents the enhanced CO column observed at the downwind site, d is the distance from the source to
184 the measuring site and v is the wind speed.

185 To estimated averaged emissions from satellite observations over a region, the wind-assigned method was applied (Tu
186 et al., 2022a, 2022b, 2023, 2024b). This technique fits the anomalies between the satellite observations and the
187 dispersion model by analyzing enhancements under opposing wind sectors. Specifically, the wind-assigned anomaly
188 is defined as the difference in observed enhancements between two opposite wind fields (e.g., E: 0°–180° and W:
189 180°–360°). A key advantage of this approach is that it inherently eliminates the uncertainty associated with
190 background concentration calculations for long-lived gases like CO, thereby significantly improving the reliability of
191 the resulting emission estimates.

192 **3. Results and discussion**

193 **3.1 Ground-based observations**

194 Figure 2 illustrates the time-series of XCO_2, XCH_4 and XCO observed by the EM27/SUN over 8 intermittent days
195 from May 25 to June 14. XCO_2 show a mean value of 426.50 ± 1.79 ppm with relatively less intraday variability

196   compared to CO. A generally lower concentration was observed on June 4 (424.64 ± 0.25 ppm), except for a slight

197   enhancement (~1.2 ppm) in the morning, which was also observed in XCH_4 (~6 ppb) and in XCO (~15 ppb).

198   The average observed XCH_4 concentration during the measurement period was 1898.45 ± 6.66 ppb. Notably, 300 km

199   to the northwest of the study site lies the largest Muli coalfield in Qinghai Province, which has an estimated coal

200   reserve of around 4 billion tons (Xiao et al., 2023). However, the maximum XCH_4 enhancement observed was

201   approximately 10 ppb on May 25, when the wind was from northwest before noon. This enhancement is relatively

202   lower than those reported in other coal fields, such as in Changzhi, Shanxi Province (Tu et al., 2024a), suggesting that

203   the ground-based observations may not have fully captured the methane emissions. The modest enhancement is likely

204   due to the relatively greater distance from the source, combined with potentially low coal mining activity during the

205   observing period, as coal production is often highly episodic.

206   XCO exhibited a mean value of 153.75 ppb and a standard deviation of 52.09 ppb. These values are significantly

207   higher than those in the Arctic and Antarctica (Pollard et al., 2022; Sha et al., 2024), as well as in urban areas such as

208   Seoul (Park et al., 2024), Xianghe near Beijing (Che et al., 2022a; Yang et al., 2020) and Hefei (Shan et al., 2022).

209   Among the investigated gases, XCO exhibits the most significant intraday variability, particularly on May 25, 27 and

210   June 14. During these days, prevailing easterly winds transported airmasses from Xining City and the nearby highway

211   (Xiong et al., 2022), leading to the elevated XCO levels. In contrast, on June 4, when airmasses primarily originated

212   from the west and northwest—regions with less urbanized areas—XCO levels were notably stable and low, averaging

213   93.93 ± 4.23 ppb (see back trajectories on Figure A 2). Additionally, higher wind speed on June 4 facilitated the

214   dispersion of CO, contributing to the lower CO level. The enhancement of XCO and XCO_2 ratio ($\Delta XCO:\Delta XCO_2$, see

215   section 3.5) exhibited slopes of 14.43 ppb/ppm before noon and 4.76 ppb/ppm in the late afternoon. Both values were

216   significantly lower than those observed under easterly wind conditions. This suggests that the CO and CO_2 emissions

217   in the western regions originate from different combustion processes or source types compared to those in the east.

218
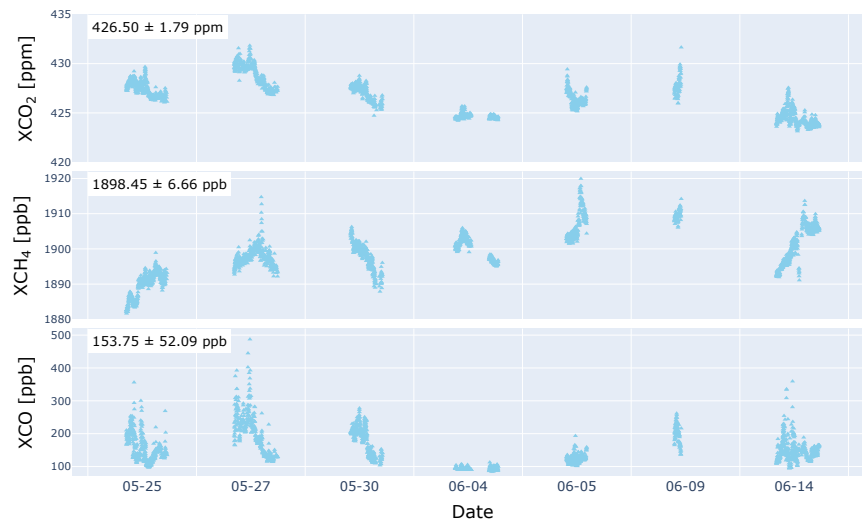
219   **Figure 2: time-series of EM27/SUN observations from May 25 to June 14 2024.**

3.2 Comparison of COCCON data with TROPOMI and IASI products

Figure 3a-b illustrates the correlations between TROPOMI and COCCON measurements on different days. The spatial collocation criterion requires the TROPOMI observations to fall within a radius of 200 km for XCH_4 and 100 km for XCO. The temporal collocation criterion is set to ±2h for COCCON measurements.

The results indicate that TROPOMI tends to slightly overestimate XCH_4 by an average bias of 8.74± 12.19 ppb, while it significantly underestimates of XCO, showing a bias of 49.49 ± 25.76 ppb. The correlation between TROPOMI and COCCON XCH_4 measurements improves as the spatial distance between their respective locations decreases. The largest observed difference in XCH_4, approximately -20.66 ppb, occurs on June 14, when the minimal distance between TROPOMI and COCCON locations is around 150 km (Figure A 3a).

A similar trend is observed for XCO, where larger biases are generally associated with greater distances. However, on May 27, the largest bias (69.23 ppb) occurs despite a relatively small minimum distance of 13 km. This significant discrepancy is likely influenced by the spatial distribution of TROPOMI observations relative to the EM27/SUN location. Notably, on May 27, TROPOMI XCO levels exhibit a negative correlation with distance for observations within approximately 100 km (Figure A 3b). The closest observation to the EM7/SUN location records a TROPOMI XCO value of 157.20 ppb, resulting in a significantly reduced bias of 16.72 ppb.

CO emissions from vehicle exhaust, a major contributor to air pollution, is closely related to fossil fuel combustion (Naus et al., 2018). Gao et al. (2025) reported that CO emissions increased significantly with altitude, observing nearly twice the emission levels in Xining (2320 m) compared to those at an altitude of 20 m. This trend can be attributed to the decline in atmospheric pressure and air density at higher elevations (Fattah et al., 2019). Under such conditions, engines draw in less air per cycle, which alters the air-fuel ratio and leads to suboptimal combustion. As altitude rises, the excess air ratio decreases because more diesel fuel is injected into the cylinders, but less air is captured per cycle. Therefore, the combustion between fresh air and diesel fuel becomes incomplete, resulting in substantial CO emissions.

The correlation between IASI and COCCON is relatively higher (R^2 = 0.6478) compared to the correlation between TROPOMI and COCCON XCO. Similar to TROPOMI, IASI shows the highest bias on May 27 with a value of 2.43E22 molec./m^2. Enhanced CO levels are observed within 20 km radius, with the peak CO concentration reaching 2.66E22 molec./m^2 at 15.4 km (Figure A 3c). As a result, the bias decreases by nearly half to 1.32E22 molec./m^2.
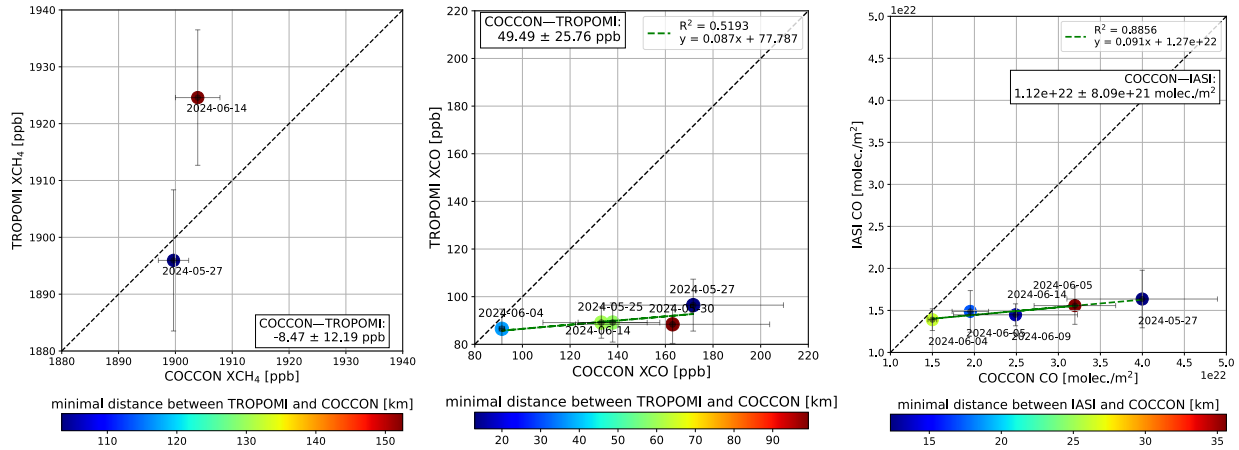
Figure 3: Correlation plot between TROPOMI and COCCON for XCH₄ (a) and XCO (b) and between IASI and COCCON for CO column (c). The colour bar represents the minimum distance between the TROPOMI and COCCON locations.

3.3 Comparison of COCCON data with CAMS products

The CAMS GHG forecast provides a high spatial resolution of approximately 9 km. For comparison with the EM27/SUN site, the following coincidence criteria were used: CAMS data nearest to the EM27/SUN location and EM27/SUN observations within ± 2h around noon.

In daily comparison, the CAMS forecast XCH_4 demonstrates a strong correlation ($R^2 = 0.7826$) with COCCON observations and an average bias of 4.21 ± 4.40 ppb. In contrast, CAMS generally underestimates both XCO_2 and the CO column, exhibiting lower correlations. The mean biases are 1.78 ± 1.47 ppm for XCO_2 and 9.97E21 ± 6.31E21 molec./m^2 for CO. The largest biases in XCO_2 and CO are recorded on May 27. This discrepancy is also observed in TROPOMI and IASI CO observations. When comprising the absolute column amounts, CAMS shows an approximately 0.4% underestimation for XCO_2 and 0.2% for XCH_4 relative to the COCCON data. However, the underestimate of CO is more pronounced, with a bias of 35%.

CAMS XCH_4 compares much better with COCCON observations than XCO_2 and XCO, as the higher value of R^2 and the better agreement of the slope of the regression line indicates. We conclude that the variability of XCO and XCO_2 dominating the variability as detected by the ground-based observation is generated on a smaller spatial scale which is not properly resolved in the simulation. In contrast, the variability of the CH_4 model field seems to be dominated by extended sources distributed in a wider area, which therefore can be properly depicted by the model.

In terms of broader implications, the relatively strong performance of CAMS in simulating CH_4, especially when compared to CO and CO_2, indicates that CAMS may be more reliable for CH_4 studies in such regions. This finding could potentially support the case for establishing long-term observation sites in this area to help with satellite validation and improve model accuracy, particularly for species like CO, which appear to require more refined simulations.

270
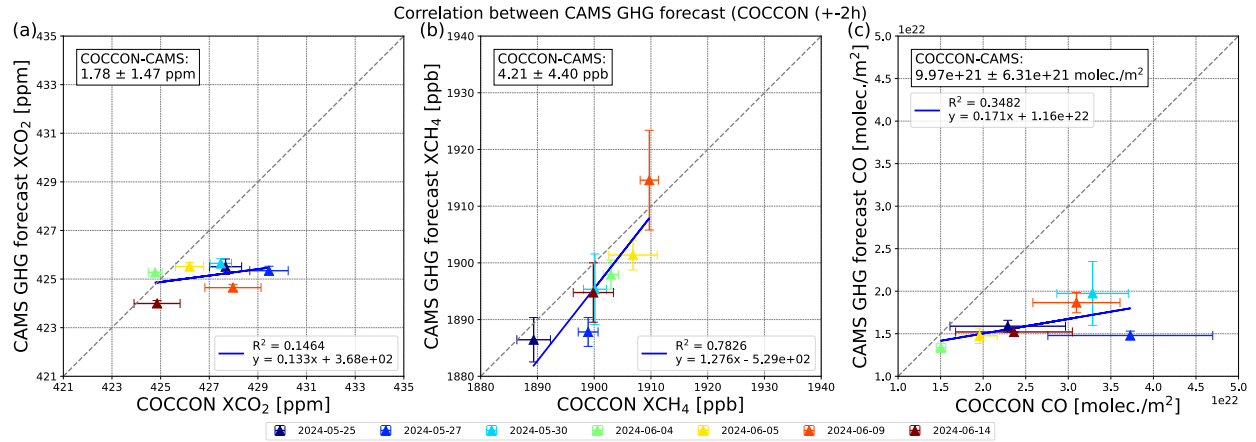
Figure 4: Correlation between CAMS forecast and COCCON for XCO$_2$ (a), XCH$_4$ (b) and CO column (c).

3.3 CO emission estimates based on ground-based observations

273 Satellite observations, such as TROPOMI and IASI, and CAMS forecasts, consistently underestimate CO levels
274 during the entire field campaign. Thus, ground-based measurements are essential for accurately estimating CO
275 emissions. Wind directions predominantly originated from the east (Figure A 1) on five days, indicating that emissions
276 from the Xining city were being transported to the downwind site where the EM27/SUN located.

277 Figure 5 highlights the correlation between ΔXCO multiplied by wind speed as a function of wind direction. ΔXCO
278 represents the emitted signals by subtracting backgrounds from the observations. The daily background is defined as
279 the lowest 10th percentile of measurements. Wind directions within the range of 80° – 120°, associated with relatively
280 higher multiplication between ΔXCO and wind speed, were selected to represent the predominant winds transporting
281 emissions from Xining. In this range, the average wind speed is approximately 2.3 m/s, with a standard deviation of
282 0.7 m/s. To account for variability, an uncertainty of ±20º is applied. The wind spreading angle ∂ is defined as:

$$\partial = 120° - 80° = 40°(\pm 20°) = 0.7\ (\pm 0.35)\ rad$$

284 Based on this wind spreading angle, the CO emission is calculated using the dispersion model in Equation 1. The
285 elevated values between 250° – 300° are mainly attributable to higher wind speeds. This sector is not the focus of the
286 present study, as the ground-based EM27/SUN instrument primarily observes air masses from Xining transported by
287 easterly winds.

288
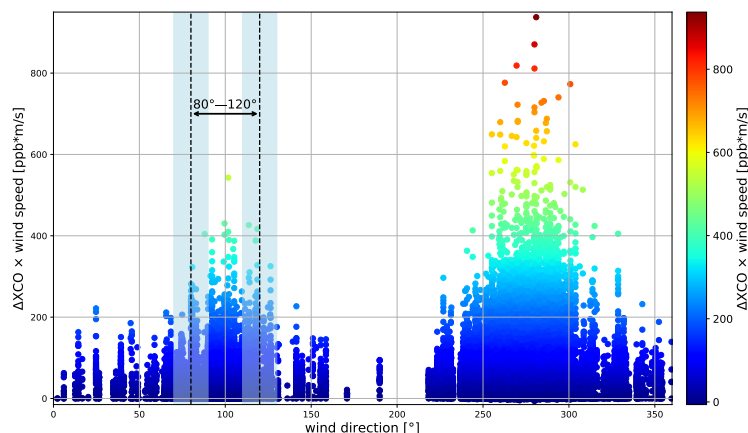
Figure 5: TROPOMI ΔXCO multiplied by wind speed against the wind direction for wind speed greater than 1.5 m/s, covering the period from May 2018 to June 2024. Wind data are derived from ERA5 at a heigh of 100m above ground level at the EM27/SUN station at 14:00 local time. The ΔXCO dataset represents XCO residuals after background subtraction. The wind direction range of 80°–120° (delineated by dashed lines) captures the predominant wind influence from Xining city. The shaded areas represent the uncertainty of ±10°.

To minimize accidental bias, a 10-minuten averaged EM27/SUN CO dataset was used. Significant enhancements are observed in ΔXCO and $ΔXCO_2$ in the 80°-120° wind direction range (Figure A 4). Using Equation (2), the estimated CO emissions for five days are presented in Figure 7. Notably, relatively high emissions were observed in the 80°-120° wind direction range, corresponding to areas of higher wind speed. A similar enhancement of CO associated with easterly winds was reported by Xiong et al. (2022), where in situ observations at the Waliguan station (36.28°N, 100.09°E, 3816 m a.s.l.), located approximately 155 km southwest of Xining city. This highlights the influence of regional air transport on the observed CO concentrations.

The CO emissions in the wind direction interval of 80°-120° are likely attributed to Xining city, with a mean estimated emission rate of 2.7E26 ± 2.1E26 molec./s (i.e., 12.3 ± 9.6 kg/s, see Figure 6). The maximum emission rate reached 1.2E27 molec./s (i.e., 55.6 kg/s) on May 27, a day when both satellite observations and forecasts underestimated the CO levels. The peak emission on May 27 occurred around noon, coinciding with a significant enhancement in XCO, which reached an approximate 10-minute averaged signal of 300 ppb.

306
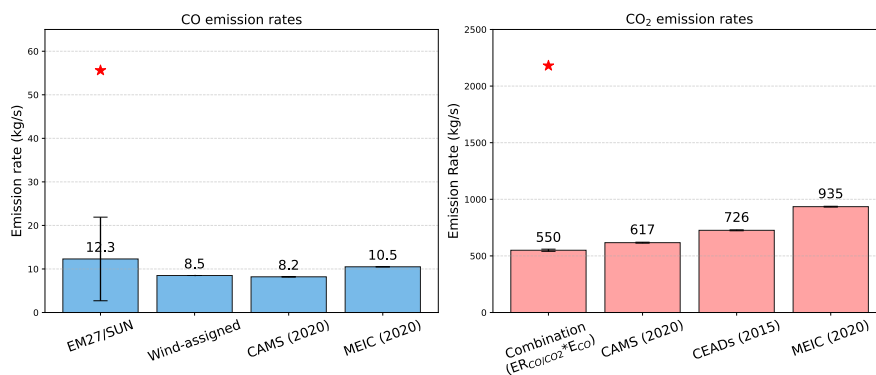
Figure 6: CO and CO₂ emissions from this study and different inventories over Xining city. The red start symbols represent the highest value derived from EM27/SUN observations.

309 Another notable high emission event was observed on May 25 and 30, under wind directions around 60°. These
310 elevated emissions are likely to attributed to emission from the north-northeast region of the EM27/SUN location. On
311 May 25, an enhanced XCO signal (~80 ppb) was observed in the late afternoon, coinciding with a relatively higher
312 wind speed of ~2.8 m/s, which contributed to the increased emissions. On March 30, the XCO signal peaked at ~120
313 ppb around noon, leading to even higher emission rates.

314
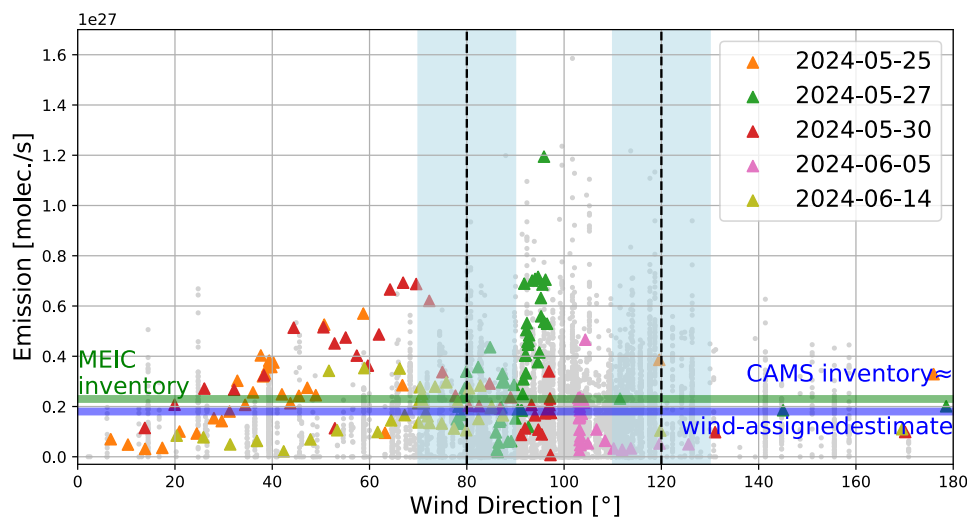
315 **Figure 7: Estimated emission relative to wind direction on six days of ground-based measurements (triangle symbols) when**
316 **winds were predominantly easterly. Grey dots represent emissions derived from TROPOMI XCO. The green horizontal**
317 **line indicates CO emission rates derived from the MEIC inventory, while the blue line represents both CAMS-GLOB-ANT**
318 **inventory and wind-assigned anomaly method estimates, which yield nearly identical values.**

319 **3.4 CO emission estimates based on satellite-based observations**

320 TROPOMI observes relative high CO levels near the central region of Xining. A distinct streak of elevated CO
321 concentrations extends eastward from Xining toward the Qinghai province border and continues toward Lanzhou in
322 Gansu province (not shown in the figure). This pattern aligns with the location of densely populated residential regions
323 and coincides with a gradual decrease in altitude from west to east (Figure A 5).

324
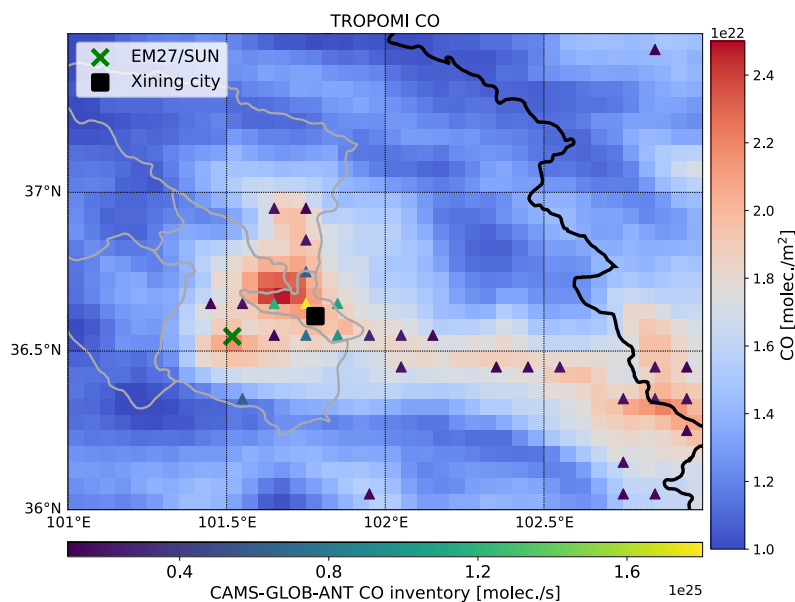
Figure 8: Spatial distribution of the average TROPOMI CO column at a latitude-longitude resolution of 0.05º, covering the period from May 2018 to June 2024. The triangle symbols indicate locations where CO emissions exceed 1E24 molec./s based on the CAMS-GLOB-ANT inventory. The green cross marks the location of the EM27/SUN and the black square represents the center of Xining city. The thick black line outlines the Qinghai province boundary and the thin grey lines delineate subregions within Xining.

Emissions derived from TROPOMI CO products, based on the Eq1. are presented in Figure 7 (grey dots), showing relatively higher values for wind directions between 80º and 120º. The average emission rate is approximately 8.9 ± 7.5 kg/s, which closely matches the emissions derived from the COCCON measurements.

To further estimate regional CO emissions, a wind-assigned method in combination with the dispersion model described in Eq.1 is applied to the TROPOMI observations. The estimated CO emission based on the wind-assigned anomaly method is approximately 1.8E26 molec./s (8.5 kg/s). This value is comparable to the CAMS-GLOB-ANT inventory (1.8E26 molec./s, i.e., 8.2 kg/s), the Multi-resolution Emission Inventory model for Climate and air pollution research (MEIC, http://meicmodel.org.cn, last access: 1 September 2025), (Geng et al., 2024; Li et al., 2017), which reports 10.5 kg/s, and the average emission derived from the six-day EM27/SUN measurements (2.7E26 molec./s, i.e., 12.3 kg/s). However, scatters are observed in the correlation between the TROPOMI and modeled wind-assigned anomalies, leading to a lower R^2 value (Figure 9). This discrepancy could originate from uncertainties in the CAMS inventory, which may not account for some some-high emission sources. Additionally, the simple dispersion model introduces its own uncertainties, which limits the ability to accurately model CO enhancements.

343
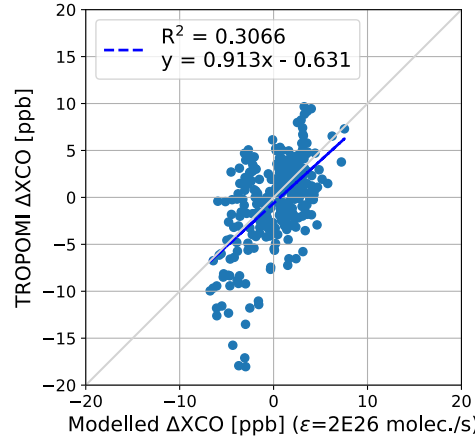
Figure 9: Correlation in the wind-assigned anomalies between the TROPOMI observations and modeled anomalies.

3.5 CO_2 estimates based on combustion efficiency

346   In urban environments, CO is primarily produced through the incomplete combustion of fossil fuels, such as those
347   from traffic emissions and industrial activities, often occurring alongside the formation of CO_2. The CO to CO_2 ratio
348   serves as a valuable indicator for atmospheric fossil-fuel CO_2 emissions and combustion efficiency, providing insights
349   into the sources and effectiveness of fuel use (Che et al., 2022b; Lee et al., 2024; Sim et al., 2020).

350   Figure 10 presents the relationship between ΔXCO and ΔXCO_2 under predominant wind of wind direction of 80° −
351   120° and wind speed larger than 1.5 m/s for different days. The daily background concentrations of XCO_2 and XCO
352   were determined as the lowest 10th percentile of the respective observations. ΔXCO and ΔXCO_2 was calculated by
353   subtracting the daily background concentrations from the daily observed values. Under easterly wind conditions,
354   ΔXCO exhibits a stronger correlation with ΔXCO_2, with a slope of 35.14 (ppb/ppm) and an R^2 value of 0.7552,
355   indicating distinct source contributions and atmospheric transport processes from eastern regions, such as Xining city.
356   The observed $\Delta XCO/\Delta XCO_2$ ratio is higher than those reported in other studies (Che et al., 2022b; Lee et al., 2024).
357   This discrepancy is attributed to significantly elevated CO levels under easterly wind conditions, suggesting lower
358   combustion efficiency in this region.

359   Using CO as a proxy, the fossil fuel-derived CO_2 emissions can be computed as follows:

$$E_{CO_2} = \left(\frac{1}{ER_{CO/CO_2}} \times \frac{M_{CO_2}}{M_{CO}}\right)E_{CO} \qquad\qquad \textbf{Eq. 2}$$

360   Where E_{CO_2} is the emissions of CO_2 in kg/s, ER_{CO/CO_2} is the ground-based observed ratio of $\Delta XCO{:}\Delta XCO_2$ in
361   ppb/ppm, E_{CO} is the CO emission rate derived from TROPOMI observations (see Sec. 3.4), and M_{CO_2} and M_{CO} are the
362   molar mass of CO_2 and CO, respectively.

363   We estimate an average CO_2 emission rate of approximately 550 kg/s, which aligns well with the CAMS-GLOB-ANT
364   (617 kg/s for 2020) though lower than the Carbon Emission Accounts and Datasets (CEADs) (726 kg/s for 2015)
365   ("Methodology and applications of city level CO2 emission accounts in China," 2017; Shan et al., 2018) and MEIC

366 (935 kg/s for 2020) estimates. The data also reveal strong daily fluctuations in emissions. The peak event was observed

367 on May 27, which exhibited a maximum $\Delta XCO{:}\Delta XCO_2$ ratio of 40.08 ($R^2 = 0.8544$). This ratio translates to a

368 maximum CO emission rate of 55.6 kg/s and a concurrent maximum CO_2 emission rate of 2180 kg/s.

369 Additionally, the CAMS and MEIC inventories show similar CO/CO_2 emission ratios of 0.021 and 0.018, respectively.

370 As detailed in Section 3.2 and 3.3, both TROPOMI and CAMS model underestimate the atmospheric CO column by

371 a factor of approximately 1.6. When we correct for this bias by scaling the TROPOMI-derived emission and CAMS

372 inventory, the resulting emission ratio increases to 0.034. This corrected value aligns closely with our observed

373 $\Delta XCO/\Delta XCO_2$ enhancement ratio of 0.035 ppb/ppb.

374 The observed discrepancies compared with inventories may be attributed to differences in temporal coverage,

375 methodological approaches, and potential changes in emission patterns over time. Additionally, it should be noted that

376 the field campaign spanned only three weeks from May to June, which mainly represents early summer. During other

377 seasons, such as summer or winter, when photosynthesis activities or coal burning for heating is more prevalent, the

378 $\Delta XCO{:}\Delta XCO_2$ ratios and associated CO_2 emissions may differ. A longer period of ground-based observations and

379 running several spectrometers upwind and downwind may improve our results. Our findings so far demonstrate the

380 potential of the EM27/SUN spectrometer as a promising tool for comprehensively evaluating greenhouse gas (GHG)

381 and air pollutant emissions in urban areas (Che et al., 2022b; Lee et al., 2024).

382
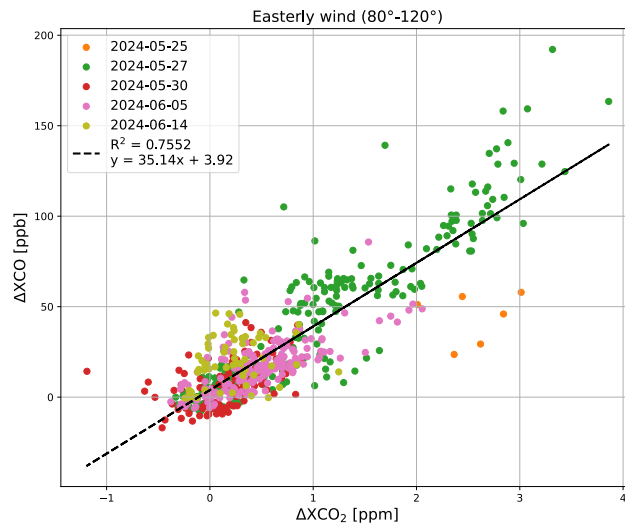
383 **Figure 10: Ground-based observed $\Delta XCO/\Delta XCO_2$ ratios under easterly wind conditions covering direction between 80°**
384 **and 120°. Different colors indicate observations from individual days.**

385 **Conclusion**

386 A three-week field campaign using a portal FTIR spectrometer (EM27/SUN) was conducted at Ganhe Industrial Park,

387 located in the southwestern suburbs of Xining city, from May 23 to June 14, 2024. The mean and standard deviation

388 values for XCO_2, XCH_4 and XCO were 426.50±1.79 ppm, 1898.45±6.66 ppb and 153.75±52.09 ppb, respectively.

389 Among these gases, XCO exhibited significant intraday variability, particularly on days dominated by easterly winds,

390 which transported airmass from Xining city.

391   Ground-based observations were compared with co-located datasets from TROPOMI, IASI and CAMS. Results
392   indicate that TROPOMI slightly overestimates XCH_4, with an average bias of 8.47 ± 12.19 ppb, but significantly
393   underestimates XCO, showing a bias of 49.49 ± 25.76 ppb. IASI generally underestimates the CO column relative to
394   COCCON observations, with an average bias of $1.12E22 \pm 8.09E21$ molec./m^2. CAMS forecasts also underestimated
395   XCO_2 (1.78 ± 1.47 ppm), XCH_4 (4.21 ± 4.40 ppb) and CO column ($9.97E21 \pm 6.31E21$ molec./m^2). A high correlation
396   (R^2=0.7930) was found for XCH_4 between CAMS and EM27/SUN datasets. The largest discrepancies in CO products
397   occurred on May 27, when significant enhancements were observed at the co-located time by EM27/SUN. These
398   discrepancies are partly attributed to satellite observations, as their concentrations decreased with distance from the
399   EM27/SUN location.

400   Wind directions predominantly originated from the east on five measurement days, indicating that emissions from the
401   Xining city were being transported to the downwind site where the EM27/SUN spectrometer was located. A simple
402   dispersion model, incorporating wind information and enhanced CO column data from EM27/SUN instrument, was
403   applied to estimate CO emissions. The CO emissions from Xining city are estimated at 12.3 ± 9.6 kg/s with a peak
404   emission rate of 55.6 kg/s on May 27, when both satellite observations and forecasts underestimated CO levels. When
405   this model was applied to TROPOMI CO data, the resulting average emission rate was 8.9 ± 7.5 kg/s. A wind-assigned
406   anomaly method was also applied to the TROPOMI CO dataset, resulting in an estimate emission rate of 8.5 kg/s.
407   Both EM27/SUN-based and TROPOMI-based estimates are comparable to the CAMS inventory value of 8.2 kg/s in
408   2020.

409   CO can serve as a proxy for fossil fuel-derived CO_2 emissions. Ground-based obversions of ΔXCO and ΔXCO_2 exhibit
410   a stronger correlation under wind direction of 80°– 120°, with a slope of 35.14 ppb/ppm and an R^2 value of 0.7552,
411   compared to conditions under westerly winds. Using these correlations, we estimated the CO_2 emission rate to have
412   an average value of 550 kg/s with a maximum value of 2180 kg/s. These estimates align reasonably with the CAMS-
413   GLOB-ANT (617 kg/s for 2020) and the CEASs inventory, which reports a CO_2 emission rate of 726kg/s for Xining
414   in 2015. Observed discrepancies may be attributed to differences in temporal coverage, methodological approaches,
415   and potential changes in emission patterns over time. Note that long-term ground-based measurements of trace gases
416   may improve the precision of estimated emissions.

417   Our findings highlight the potential of the EM27/SUN spectrometer as a valuable tool for detecting local emission
418   and supporting satellite validation, particularly in high-altitude regions such as Tibetan Plateau. This study establishes
419   a novel approach for estimating CO_2 emissions by synergistically combining ground-based and space-based
420   measurements. While TROPOMI provides extensive spatial coverage for CO, the lack of direct CO_2 measurements
421   from this platform—coupled with the sparse coverage of dedicated CO_2 satellites (OCO-2/3, GOSAT) in this region—
422   highlights a critical observational gap. The simultaneous measurement of columnar CO and CO_2 by EM27/SUN
423   provides a key advantage, enabling direct correlation of their emissions and offering a cost-effective approach for
424   comprehensive greenhouse gas and air pollutant assessment.

425

426 **Data availability.**

427 The TROPOMI CH_4 and CO dataset is a Copernicus operational product and is available at
428 https://doi.org/10.5270/S5P-3lcdqiv (Copernicus Sentinel-5P, 2021). The access and use of any Copernicus Sentinel
429 data available through the Copernicus Open Access Hub are governed by the legal notice on the use of Copernicus
430 Sentinel Data and Service Information, which is given at
431 https://sentinels.copernicus.eu/documents/247904/690755/Sentinel_Data_Legal_Notice (last access: January 2025).
432 IASI CO dataset is available at https://iasi.aeris-data.fr/co/ (last access: January 2025). CAMS forecasts are
433 available at 10.24381/93910310 (last access: January 2025) and CAMS-GLOB-ANT inventory data are available at
434 https://doi.org/10.24380/eets-qd81 (last access: January 2025). CEADS inventory is available at:
435 https://www.ceads.net/data/city?#1280. last access: January 2024.

436 **Author contributions.**

437 QT and FH conceived the research question. QT wrote the manuscript and conducted the data analysis with input from
438 FH. XL and ZY carried out the measurements, while YJ and JF was responsible for the data processing. All authors
439 contributed to the interpretation of the results and the improvement of the paper.

440 **Declaration of Competing Interest.**

441 The authors declare that they have no known competing financial interests or personal relationships that could have
442 appeared to influence the work reported in this paper.

443 **Acknowledgements.**

444 We would like to thank Copernicus User Support Team at ECMWF for providing the CAMS model data. We thank
445 the TROPOMI team for making CH_4 and CO data and IASI team for CO data publicly available.

446 **Financial support.**

447 This research was funded by the National Natural Science Foundation of China (grant no. 42305138) and the National
448 Key Research and Development Program (2022YFE0209500).

449

450 **Appendix**
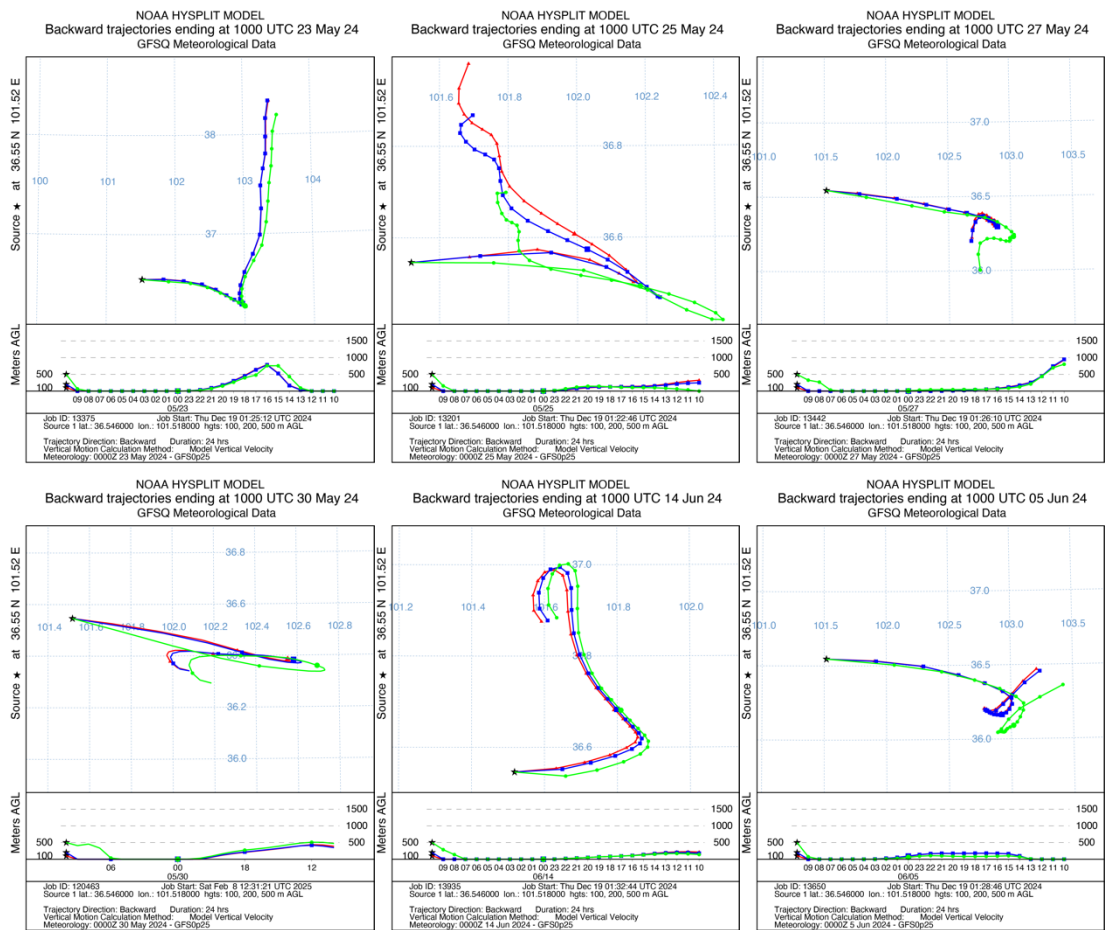
453 **Figure A 1 The back trajectories originating from eastern areas and arriving at EM27/SUN station at 10 UTC (18 Local**
454 **time) on different days. The trajectories, calculated using the HYSPLIT model (Hybrid Single-Particle Lagrangian**
455 **Integrated Trajectory), and shown for height of 100, 200 and 500 m above ground level.**

457 **Figure A 2 Similar to Figure A 1, but for trajectories generally from western areas on June 4 and 9, 2024.**

458
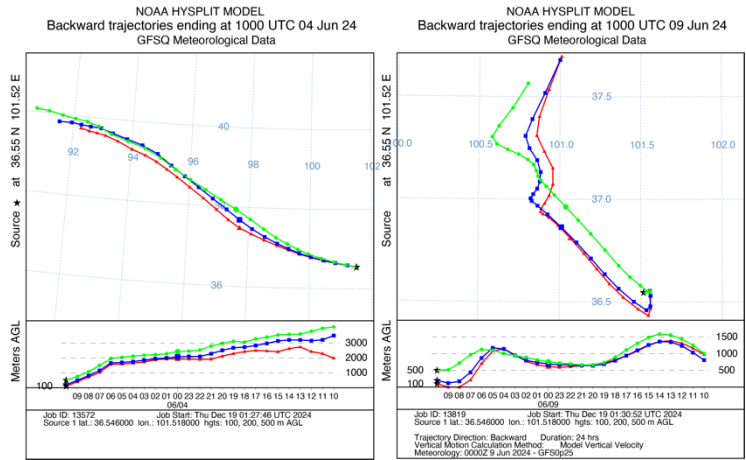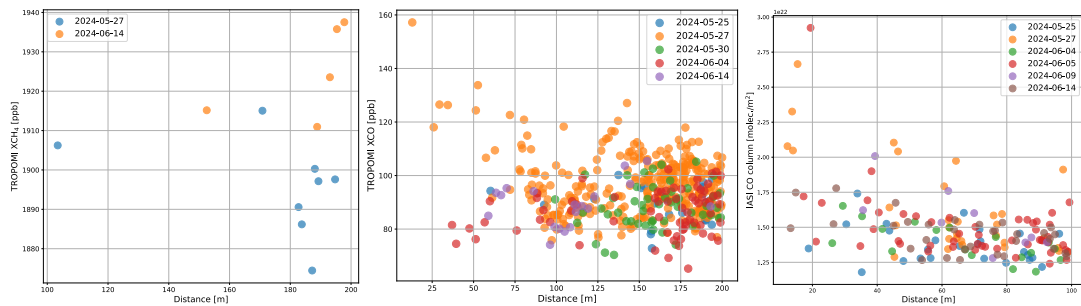
Figure A 3: Correlation between TROPOMI XCH₄ (a) and XCO (b) with the distance from each TROPOMI observation to the EM27/SUN location. Panel (c) shows the correlation between IASI CO and the distance from each IASI observation to the EM27/SUN location.

462
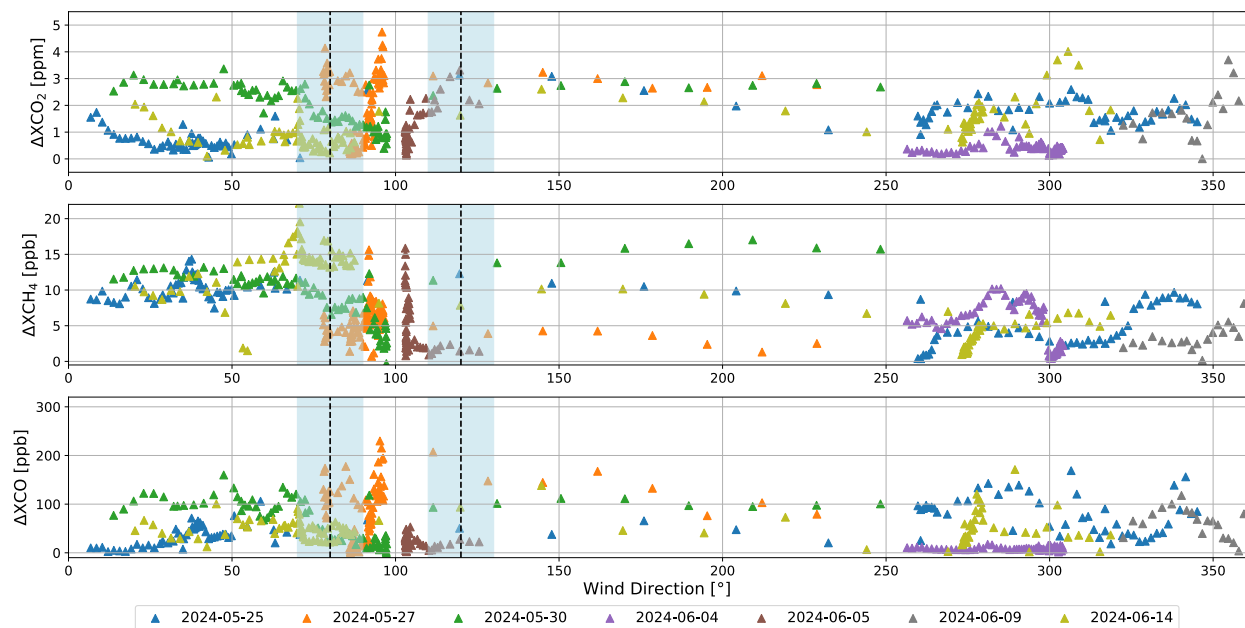
Figure A 4: correlations between ΔXCO₂, ΔXCH₄ and ΔXCO with wind direction. The wind direction range of 80°-120° is delineated by dashed lines.

465
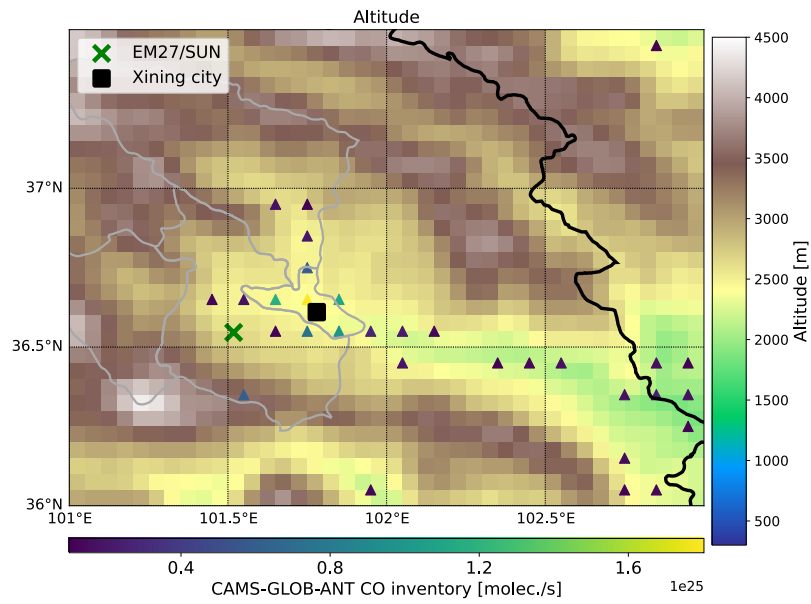
Figure A 5: similar to Figure 8 but for terrain distribution.

467

Reference

Holm, E., Forbes, R., Lang, S., Magnusson, L., and Malardel, S.: New model cycle brings higher resolution, ECMWF Newsletter, ECMWF, Reading UK, No. 147, available at: https://www.ecmwf.int/en/elibrary/16299-newsletter-no-147-spring-2016 (last access: Januray 2024), 2016.

Xining Statistical Bureau. Xining statistical yearbook. 2001. 2021-11-26. https://tjj.xining.gov.cn/zwgk/fdzdgknr/tjxx/gjnj/202111/t20211126_159614.html.

IPCC. (2007). In S. Solomon, D. Qin, M. Manning, Z. Chen, M. Marquis, K. B. Averyt, et al. (Eds.), Climate Change 2007: The Physical Science Basis. Contribution of Working Group I to the Fourth Assessment Report of the International Panel on Climate Change (p. 996). Cambridge University Press.

Carbon Emission Accounts and Datasets (CEADs), 2018. The Emission Inventories for 290 Chinese Cities from 1997 to 2019. available at: https://www.ceads.net/data/city?#1280. last access: January 2024.

Agusti-Panareda, A., Diamantakis, M., Bayona, V., Klappenbach, F., Butz, A., 2017. Improving the inter-hemispheric gradient of total column atmospheric CO_2 and CH_4 in simulations with the ECMWF semi-Lagrangian atmospheric global model. Geoscientific Model Development 10, 1–18. https://doi.org/10.5194/gmd-10-1-2017

Agustí-Panareda, A., Diamantakis, M., Massart, S., Chevallier, F., Muñoz-Sabater, J., Barré, J., Curcoll, R., Engelen, R., Langerock, B., Law, R.M., Loh, Z., Morguí, J.A., Parrington, M., Peuch, V.-H., Ramonet, M., Roehl, C., Vermeulen, A.T., Warneke, T., Wunch, D., 2019. Modelling CO_2 weather – why horizontal resolution matters. Atmospheric Chemistry and Physics 19, 7347–7376. https://doi.org/10.5194/acp-19-7347-2019

Agustí-Panareda, A., Massart, S., Chevallier, F., Boussetta, S., Balsamo, G., Beljaars, A., Ciais, P., Deutscher, N.M., Engelen, R., Jones, L., Kivi, R., Paris, J.-D., Peuch, V.-H., Sherlock, V., Vermeulen, A.T., Wennberg, P.O., Wunch, D., 2014. Forecasting global atmospheric CO_2. Atmospheric Chemistry and Physics 14, 11959–11983. https://doi.org/10.5194/acp-14-11959-2014

Alberti, C., Hase, F., Frey, M., Dubravica, D., Blumenstock, T., Dehn, A., Castracane, P., Surawicz, G., Harig, R., Baier, B.C., Bès, C., Bi, J., Boesch, H., Butz, A., Cai, Z., Chen, J., Crowell, S.M., Deutscher, N.M., Ene, D., Franklin, J.E., García, O., Griffith, D., Grouiez, B., Grutter, M., Hamdouni, A., Houweling, S., Humpage, N., Jacobs, N., Jeong, S., Joly, L., Jones, N.B., Jouglet, D., Kivi, R., Kleinschek, R., Lopez, M., Medeiros, D.J., Morino, I., Mostafavipak, N., Müller, A., Ohyama, H., Palmer, P.I., Pathakoti, M., Pollard, D.F., Raffalski, U., Ramonet, M., Ramsay, R., Sha, M.K., Shiomi, K., Simpson, W., Stremme, W., Sun, Y., Tanimoto, H., Té, Y., Tsidu, G.M., Velazco, V.A., Vogel, F., Watanabe, M., Wei, C., Wunch, D., Yamasoe, M., Zhang, L., Orphal, J., 2022. Improved calibration procedures for the EM27/SUN spectrometers of the COllaborative Carbon Column Observing Network (COCCON). Atmospheric Measurement Techniques 15, 2433–2463. https://doi.org/10.5194/amt-15-2433-2022

Babenhauserheide, A., Hase, F., Morino, I., 2020. Net CO_2 fossil fuel emissions of Tokyo estimated directly from measurements of the Tsukuba TCCON site and radiosondes. Atmospheric Measurement Techniques 13, 2697–2710. https://doi.org/10.5194/amt-13-2697-2020

Bian, J., Li, D., Bai, Z., Li, Q., Lyu, D., Zhou, X., 2020. Transport of Asian surface pollutants to the global stratosphere from the Tibetan Plateau region during the Asian summer monsoon. National Science Review 7, 516–533. https://doi.org/10.1093/nsr/nwaa005

Butz, A., Hasekamp, O.P., Frankenberg, C., Aben, I., 2009. Retrievals of atmospheric CO_2 from simulated space-borne measurements of backscattered near-infrared sunlight: accounting for aerosol effects. Appl. Opt., AO 48, 3322–3336. https://doi.org/10.1364/AO.48.003322

Callewaert, S., Brioude, J., Langerock, B., Duflot, V., Fonteyn, D., Müller, J.-F., Metzger, J.-M., Hermans, C., Kumps, N., Ramonet, M., Lopez, M., Mahieu, E., De Mazière, M., 2022. Analysis of CO_2, CH_4, and CO surface and column concentrations observed at Réunion Island by assessing WRF-Chem simulations. Atmospheric Chemistry and Physics 22, 7763–7792. https://doi.org/10.5194/acp-22-7763-2022

Che, K., Liu, Y., Cai, Z., Yang, D., Wang, H., Ji, D., Yang, Y., Wang, P., 2022a. Characterization of Regional Combustion Efficiency using ΔXCO: ΔXCO2 Observed by a Portable Fourier-Transform Spectrometer at an Urban Site in Beijing. Adv. Atmos. Sci. 39, 1299–1315. https://doi.org/10.1007/s00376-022-1247-7

Che, K., Liu, Y., Cai, Z., Yang, D., Wang, H., Ji, D., Yang, Y., Wang, P., 2022b. Characterization of Regional Combustion Efficiency using ΔXCO: ΔXCO2 Observed by a Portable Fourier-Transform Spectrometer at an Urban Site in Beijing. Adv. Atmos. Sci. 39, 1299–1315. https://doi.org/10.1007/s00376-022-1247-7

Chen, J., Dietrich, F., Maazallahi, H., Forstmaier, A., Winkler, D., Hofmann, M.E.G., Denier van der Gon, H., Röckmann, T., 2020. Methane emissions from the Munich Oktoberfest. Atmospheric Chemistry and Physics 20, 3683–3696. https://doi.org/10.5194/acp-20-3683-2020

Clerbaux, C., Boynard, A., Clarisse, L., George, M., Hadji-Lazaro, J., Herbin, H., Hurtmans, D., Pommier, M., Razavi, A., Turquety, S., Wespes, C., Coheur, P.-F., 2009. Monitoring of atmospheric composition using the thermal infrared IASI/MetOp sounder. Atmospheric Chemistry and Physics 9, 6041–6054. https://doi.org/10.5194/acp-9-6041-2009

Crippa, M., Guizzardi, D., Pisoni, E., Solazzo, E., Guion, A., Muntean, M., Florczyk, A., Schiavina, M., Melchiorri, M., Hutfilter, A.F., 2021. Global anthropogenic emissions in urban areas: patterns, trends, and challenges. Environ. Res. Lett. 16, 074033. https://doi.org/10.1088/1748-9326/ac00e2

Dils, B., Cui, J., Henne, S., Mahieu, E., Steinbacher, M., De Mazière, M., 2011. 1997–2007 CO trend at the high Alpine site Jungfraujoch: a comparison between NDIR surface in situ and FTIR remote sensing observations. Atmospheric Chemistry and Physics 11, 6735–6748. https://doi.org/10.5194/acp-11-6735-2011

Eskes, H., Tsikerdekis, A., Ades, M., Alexe, M., Benedictow, A.C., Bennouna, Y., Blake, L., Bouarar, I., Chabrillat, S., Engelen, R., Errera, Q., Flemming, J., Garrigues, S., Griesfeller, J., Huijnen, V., Ilić, L., Inness, A.,

535   Kapsomenakis, J., Kipling, Z., Langerock, B., Mortier, A., Parrington, M., Pison, I., Pitkänen, M., Remy, S.,
536   Richter, A., Schoenhardt, A., Schulz, M., Thouret, V., Warneke, T., Zerefos, C., Peuch, V.-H., 2024.
537   Technical note: Evaluation of the Copernicus Atmosphere Monitoring Service Cy48R1 upgrade of June 2023.
538   Atmospheric Chemistry and Physics 24, 9475–9514. https://doi.org/10.5194/acp-24-9475-2024

539 Fattah, I.M.R., Yip, H.L., Jiang, Z., Yuen, A.C.Y., Yang, W., Medwell, P.R., Kook, S., Yeoh, G.H., Chan, Q.N., 2019.
540   Effects of flame-plane wall impingement on diesel combustion and soot processes. Fuel 255, 115726.
541   https://doi.org/10.1016/j.fuel.2019.115726

542 Flemming, J., Huijnen, V., Arteta, J., Bechtold, P., Beljaars, A., Blechschmidt, A.-M., Diamantakis, M., Engelen, R.J.,
543   Gaudel, A., Inness, A., Jones, L., Josse, B., Katragkou, E., Marecal, V., Peuch, V.-H., Richter, A., Schultz,
544   M.G., Stein, O., Tsikerdekis, A., 2015. Tropospheric chemistry in the Integrated Forecasting System of
545   ECMWF. Geoscientific Model Development 8, 975–1003. https://doi.org/10.5194/gmd-8-975-2015

546 Frey, M., Hase, F., Blumenstock, T., Groß, J., Kiel, M., Mengistu Tsidu, G., Schäfer, K., Sha, M.K., Orphal, J., 2015.
547   Calibration and instrumental line shape characterization of a set of portable FTIR spectrometers for detecting
548   greenhouse gas emissions. Atmos. Meas. Tech. 8, 3047–3057. https://doi.org/10.5194/amt-8-3047-2015

549 Frey, M., Sha, M.K., Hase, F., Kiel, M., Blumenstock, T., Harig, R., Surawicz, G., Deutscher, N.M., Shiomi, K.,
550   Franklin, J.E., Bösch, H., Chen, J., Grutter, M., Ohyama, H., Sun, Y., Butz, A., Mengistu Tsidu, G., Ene, D.,
551   Wunch, D., Cao, Z., Garcia, O., Ramonet, M., Vogel, F., Orphal, J., 2019. Building the COllaborative Carbon
552   Column Observing Network (COCCON): long-term stability and ensemble performance of the EM27/SUN
553   Fourier transform spectrometer. Atmos. Meas. Tech. 12, 1513–1530. https://doi.org/10.5194/amt-12-1513-
554   2019

555 Gao, H., Wang, R., Wen, Z., Xiong, X., Zheng, Z., Lin, S., Ding, H., Tan, W., 2025. The real driving emissions
556   characteristics of light-duty diesel vehicle in four typical cities with varying altitudes in China. Case Studies
557   in Thermal Engineering 67, 105831. https://doi.org/10.1016/j.csite.2025.105831

558 Geng, G., Liu, Yuxi, Liu, Yang, Liu, S., Cheng, J., Yan, L., Wu, N., Hu, H., Tong, D., Zheng, B., Yin, Z., He, K.,
559   Zhang, Q., 2024. Efficacy of China's clean air actions to tackle PM2.5 pollution between 2013 and 2020.
560   Nat. Geosci. 17, 987–994. https://doi.org/10.1038/s41561-024-01540-z

561 George, M., Clerbaux, C., Hurtmans, D., Turquety, S., Coheur, P.-F., Pommier, M., Hadji-Lazaro, J., Edwards, D.P.,
562   Worden, H., Luo, M., Rinsland, C., McMillan, W., 2009. Carbon monoxide distributions from the
563   IASI/METOP mission: evaluation with other space-borne remote sensors. Atmospheric Chemistry and
564   Physics 9, 8317–8330. https://doi.org/10.5194/acp-9-8317-2009

565 Gisi, M., Hase, F., Dohe, S., Blumenstock, T., Simon, A., Keens, A., 2012. XCO2-measurements with a tabletop FTS
566   using solar absorption spectroscopy. Atmos. Meas. Tech. 5, 2969–2980. https://doi.org/10.5194/amt-5-2969-
567   2012

568   Griffin, D., Chen, J., Anderson, K., Makar, P., McLinden, C.A., Dammers, E., Fogal, A., 2024. Biomass burning CO
569   emissions: exploring insights through TROPOMI-derived emissions and emission coefficients. Atmospheric
570   Chemistry and Physics 24, 10159–10186. https://doi.org/10.5194/acp-24-10159-2024

571   Guo, M., Fang, S., Liu, S., Liang, M., Wu, H., Yang, L., Li, Z., Liu, P., Zhang, F., 2020. Comparison of Atmospheric
572   CO2, CH4, and CO at Two Stations in the Tibetan Plateau of China. Earth and Space Science 7,
573   e2019EA001051. https://doi.org/10.1029/2019EA001051

574   Hase, F., Blumenstock, T., Paton-Walsh, C., 1999. Analysis of the instrumental line shape of high-resolution Fourier
575   transform IR spectrometers with gas cell measurements and new retrieval software. Appl. Opt. 38, 3417–
576   3422. https://doi.org/10.1364/AO.38.003417

577   Hase, F., Frey, M., Blumenstock, T., Groß, J., Kiel, M., Kohlhepp, R., Mengistu Tsidu, G., Schäfer, K., Sha, M.K.,
578   Orphal, J., 2015. Application of portable FTIR spectrometers for detecting greenhouse gas emissions of the
579   major city Berlin. Atmos. Meas. Tech. 8, 3059–3068. https://doi.org/10.5194/amt-8-3059-2015

580   Hase, F., Frey, M., Kiel, M., Blumenstock, T., Harig, R., Keens, A., Orphal, J., 2016. Addition of a channel for XCO
581   observations to a portable FTIR spectrometer for greenhouse gas measurements. Atmos. Meas. Tech. 9,
582   2303–2313. https://doi.org/10.5194/amt-9-2303-2016

583   Hasekamp, O.P., Butz, A., 2008. Efficient calculation of intensity and polarization spectra in vertically
584   inhomogeneous scattering and absorbing atmospheres. Journal of Geophysical Research: Atmospheres 113.
585   https://doi.org/10.1029/2008JD010379

586   Herkommer, B., Alberti, C., Castracane, P., Chen, J., Dehn, A., Dietrich, F., Deutscher, N.M., Frey, M.M., Groß, J.,
587   Gillespie, L., Hase, F., Morino, I., Pak, N.M., Walker, B., Wunch, D., 2024. Using a portable FTIR
588   spectrometer to evaluate the consistency of Total Carbon Column Observing Network (TCCON)
589   measurements on a global scale: the Collaborative Carbon Column Observing Network (COCCON) travel
590   standard. Atmospheric Measurement Techniques 17, 3467–3494. https://doi.org/10.5194/amt-17-3467-2024

591   Hurtmans, D., Coheur, P.-F., Wespes, C., Clarisse, L., Scharf, O., Clerbaux, C., Hadji-Lazaro, J., George, M., Turquety,
592   S., 2012. FORLI radiative transfer and retrieval code for IASI. Journal of Quantitative Spectroscopy and
593   Radiative Transfer, Three Leaders in Spectroscopy 113, 1391–1408.
594   https://doi.org/10.1016/j.jqsrt.2012.02.036

595   Kang, Y., Choi, H., Im, J., Park, S., Shin, M., Song, C.-K., Kim, S., 2021. Estimation of surface-level NO2 and O3
596   concentrations using TROPOMI data and machine learning over East Asia. Environmental Pollution 288,
597   117711. https://doi.org/10.1016/j.envpol.2021.117711

598   Landgraf, J., aan de Brugh, J., Scheepmaker, R., Borsdorff, T., Hu, H., Houweling, S., Butz, A., Aben, I., Hasekamp,
599   O., 2016. Carbon monoxide total column retrievals from TROPOMI shortwave infrared measurements.
600   Atmospheric Measurement Techniques 9, 4955–4975. https://doi.org/10.5194/amt-9-4955-2016

601   Lee, J., Jeong, S., Park, H., Hong, J., Kim, J., Frey, M.M., Morino, I., Ohyama, H., Hase, F., Mermigkas, M., Zhou,
602   M., Té, Y., Roehl, C.M., 2024. Emission Characteristics of Greenhouse Gases and Air Pollutants in Northern
603   Hemisphere Cities: Comprehensive Assessment Using Ground-Based Fourier Transform Spectrometers.
604   Journal   of   Geophysical   Research: Atmospheres   129,   e2023JD040562.
605   https://doi.org/10.1029/2023JD040562

606   Li, M., Liu, H., Geng, G., Hong, C., Liu, F., Song, Y., Tong, D., Zheng, B., Cui, H., Man, H., Zhang, Q., He, K., 2017.
607   Anthropogenic   emission   inventories   in   China: a   review.   Natl   Sci   Rev   4,   834–866.
608   https://doi.org/10.1093/nsr/nwx150

609   Luther, A., Kleinschek, R., Scheidweiler, L., Defratyka, S., Stanisavljevic, M., Forstmaier, A., Dandocsi, A., Wolff,
610   S., Dubravica, D., Wildmann, N., Kostinek, J., Jöckel, P., Nickl, A.-L., Klausner, T., Hase, F., Frey, M.,
611   Chen, J., Dietrich, F., Nęcki, J., Swolkień, J., Fix, A., Roiger, A., Butz, A., 2019. Quantifying CH_4 emissions
612   from hard coal mines using mobile sun-viewing Fourier transform spectrometry. Atmospheric Measurement
613   Techniques 12, 5217–5230. https://doi.org/10.5194/amt-12-5217-2019

614   Methodology and applications of city level CO2 emission accounts in China, 2017. . Journal of Cleaner Production
615   161, 1215–1225. https://doi.org/10.1016/j.jclepro.2017.06.075

616   Naus, S., Röckmann, T., Popa, M.E., 2018. The isotopic composition of CO in vehicle exhaust. Atmospheric
617   Environment 177, 132–142. https://doi.org/10.1016/j.atmosenv.2018.01.015

618   Park, H., Jeong, S., Sha, M.K., Lee, J., Frey, M.M., 2024. Comparisons of Greenhouse Gas Observation Satellite
619   Performances Over Seoul Using a Portable Ground-Based Spectrometer. Geophysical Research Letters 51,
620   e2024GL109334. https://doi.org/10.1029/2024GL109334

621   Pollard, D.F., Hase, F., Sha, M.K., Dubravica, D., Alberti, C., Smale, D., 2022. Retrievals of X_{CO2}, X_{CH4} and X_{CO} from
622   portable, near-infrared Fourier transform spectrometer solar observations in Antarctica. Earth System
623   Science Data 14, 5427–5437. https://doi.org/10.5194/essd-14-5427-2022

624   Sha, M.K., De Mazière, M., Notholt, J., Blumenstock, T., Bogaert, P., Cardoen, P., Chen, H., Desmet, F., García, O.,
625   Griffith, D.W.T., Hase, F., Heikkinen, P., Herkommer, B., Hermans, C., Jones, N., Kivi, R., Kumps, N.,
626   Langerock, B., Macleod, N.A., Makkor, J., Markert, W., Petri, C., Tu, Q., Vigouroux, C., Weidmann, D.,
627   Zhou, M., 2024. Fiducial Reference Measurement for Greenhouse Gases (FRM4GHG). Remote Sensing 16,
628   3525. https://doi.org/10.3390/rs16183525

629   Shan, C., Wang, W., Xie, Y., Wu, P., Xu, J., Zeng, X., Zha, L., Zhu, Q., Sun, Y., Hu, Q., Liu, C., Jones, N., 2022.
630   Observations of atmospheric CO2 and CO based on in-situ and ground-based remote sensing measurements
631   at   Hefei   site,   China.   Science   of   The   Total   Environment   851,   158188.
632   https://doi.org/10.1016/j.scitotenv.2022.158188

Shan, Y., Guan, D., Hubacek, K., Zheng, B., Davis, S.J., Jia, L., Liu, J., Liu, Z., Fromer, N., Mi, Z., Meng, J., Deng, X., Li, Y., Lin, J., Schroeder, H., Weisz, H., Schellnhuber, H.J., 2018. City-level climate change mitigation in China. Science Advances 4, eaaq0390. https://doi.org/10.1126/sciadv.aaq0390

Sim, S., Jeong, S., Park, H., Park, C., Kwak, K.-H., Lee, S.-B., Kim, C.H., Lee, S., Chang, J.S., Kang, H., Woo, J.-H., 2020. Co-benefit potential of urban CO_2 and air quality monitoring: A study on the first mobile campaign and building monitoring experiments in Seoul during the winter. Atmospheric Pollution Research 11, 1963–1970. https://doi.org/10.1016/j.apr.2020.08.009

Soulie, A., Granier, C., Darras, S., Zilbermann, N., Doumbia, T., Guevara, M., Jalkanen, J.-P., Keita, S., Liousse, C., Crippa, M., Guizzardi, D., Hoesly, R., Smith, S.J., 2024. Global anthropogenic emissions (CAMS-GLOB-ANT) for the Copernicus Atmosphere Monitoring Service simulations of air quality forecasts and reanalyses. Earth System Science Data 16, 2261–2279. https://doi.org/10.5194/essd-16-2261-2024

Spivakovsky, C.M., Logan, J.A., Montzka, S.A., Balkanski, Y.J., Foreman-Fowler, M., Jones, D.B.A., Horowitz, L.W., Fusco, A.C., Brenninkmeijer, C. a. M., Prather, M.J., Wofsy, S.C., McElroy, M.B., 2000. Three-dimensional climatological distribution of tropospheric OH: Update and evaluation. Journal of Geophysical Research: Atmospheres 105, 8931–8980. https://doi.org/10.1029/1999JD901006

Thompson, A.M., 1992. The Oxidizing Capacity of the Earth's Atmosphere: Probable Past and Future Changes | Science [WWW Document]. URL https://www.science.org/doi/10.1126/science.256.5060.1157 (accessed 12.29.24).

Tu, Q., Hase, F., Blumenstock, T., Kivi, R., Heikkinen, P., Sha, M.K., Raffalski, U., Landgraf, J., Lorente, A., Borsdorff, T., Chen, H., Dietrich, F., Chen, J., 2020. Intercomparison of atmospheric CO_2 and CH_4 abundances on regional scales in boreal areas using Copernicus Atmosphere Monitoring Service (CAMS) analysis, COllaborative Carbon Column Observing Network (COCCON) spectrometers, and Sentinel-5 Precursor satellite observations. Atmospheric Measurement Techniques 13, 4751–4771. https://doi.org/10.5194/amt-13-4751-2020

Tu, Q., Hase, F., Blumenstock, T., Schneider, M., Schneider, A., Kivi, R., Heikkinen, P., Ertl, B., Diekmann, C., Khosrawi, F., Sommer, M., Borsdorff, T., Raffalski, U., 2021. Intercomparison of arctic XH_2O observations from three ground-based Fourier transform infrared networks and application for satellite validation. Atmospheric Measurement Techniques 14, 1993–2011. https://doi.org/10.5194/amt-14-1993-2021

Tu, Q., Hase, F., Chen, Z., Schneider, M., García, O., Khosrawi, F., Chen, S., Blumenstock, T., Liu, F., Qin, K., Cohen, J., He, Q., Lin, S., Jiang, H., Fang, D., 2023. Estimation of NO_2 emission strengths over Riyadh and Madrid from space from a combination of wind-assigned anomalies and a machine learning technique. Atmospheric Measurement Techniques 16, 2237–2262. https://doi.org/10.5194/amt-16-2237-2023

Tu, Q., Hase, F., Qin, K., Alberti, C., Lu, F., Bian, Z., Cao, L., Fang, J., Gu, J., Guan, L., Jiang, Y., Kang, H., Liu, W., Liu, Y., Lu, L., Shan, Y., Si, Y., Xu, Q., Ye, C., 2024a. COCCON Measurements of XCO2, XCH4 and XCO

over Coal Mine Aggregation Areas in Shanxi, China, and Comparison to TROPOMI and CAMS Datasets. Remote Sensing 16, 4022. https://doi.org/10.3390/rs16214022

Tu, Q., Hase, F., Qin, K., Cohen, J.B., Khosrawi, F., Zou, X., Schneider, M., Lu, F., 2024b. Quantifying CH_4 emissions from coal mine aggregation areas in Shanxi, China, using TROPOMI observations and the wind-assigned anomaly method. Atmospheric Chemistry and Physics 24, 4875–4894. https://doi.org/10.5194/acp-24-4875-2024

Tu, Q., Hase, F., Schneider, M., García, O., Blumenstock, T., Borsdorff, T., Frey, M., Khosrawi, F., Lorente, A., Alberti, C., Bustos, J.J., Butz, A., Carreño, V., Cuevas, E., Curcoll, R., Diekmann, C.J., Dubravica, D., Ertl, B., Estruch, C., León-Luis, S.F., Marrero, C., Morgui, J.-A., Ramos, R., Scharun, C., Schneider, C., Sepúlveda, E., Toledano, C., Torres, C., 2022a. Quantification of CH_4 emissions from waste disposal sites near the city of Madrid using ground- and space-based observations of COCCON, TROPOMI and IASI. Atmospheric Chemistry and Physics 22, 295–317. https://doi.org/10.5194/acp-22-295-2022

Tu, Q., Schneider, M., Hase, F., Khosrawi, F., Ertl, B., Necki, J., Dubravica, D., Diekmann, C.J., Blumenstock, T., Fang, D., 2022b. Quantifying CH_4 emissions in hard coal mines from TROPOMI and IASI observations using the wind-assigned anomaly method. Atmospheric Chemistry and Physics 22, 9747–9765. https://doi.org/10.5194/acp-22-9747-2022

Veefkind, J.P., Aben, I., McMullan, K., Förster, H., de Vries, J., Otter, G., Claas, J., Eskes, H.J., de Haan, J.F., Kleipool, Q., van Weele, M., Hasekamp, O., Hoogeveen, R., Landgraf, J., Snel, R., Tol, P., Ingmann, P., Voors, R., Kruizinga, B., Vink, R., Visser, H., Levelt, P.F., 2012. TROPOMI on the ESA Sentinel-5 Precursor: A GMES mission for global observations of the atmospheric composition for climate, air quality and ozone layer applications. Remote Sensing of Environment, The Sentinel Missions - New Opportunities for Science 120, 70–83. https://doi.org/10.1016/j.rse.2011.09.027

Wunch, D., Toon, G.C., Blavier, J.-F.L., Washenfelder, R.A., Notholt, J., Connor, B.J., Griffith, D.W.T., Sherlock, V., Wennberg, P.O., 2011. The Total Carbon Column Observing Network. Philosophical Transactions of the Royal Society A: Mathematical, Physical and Engineering Sciences 369, 2087–2112. https://doi.org/10.1098/rsta.2010.0240

Xiao, W., Guo, J., He, T., Lei, K., Deng, X., 2023. Assessing the ecological impacts of opencast coal mining in Qinghai-Tibet Plateau-a case study in Muli coal field, China. Ecological Indicators 153, 110454. https://doi.org/10.1016/j.ecolind.2023.110454

Xiong, H., Lin, Y., Liu, S., Zang, K., Chen, Y., Liu, P., Liang, M., Jiang, K., Qing, X., Qiu, S., Hong, H., Li, J., Fang, S., 2022. Variations of atmospheric CO concentration from 2004 to 2019 at the Mt. Waliguan station in China. Atmospheric Research 271, 106060. https://doi.org/10.1016/j.atmosres.2022.106060

Yang, Y., Zhou, M., Langerock, B., Sha, M.K., Hermans, C., Wang, T., Ji, D., Vigouroux, C., Kumps, N., Wang, G., De Mazière, M., Wang, P., 2020. New ground-based Fourier-transform near-infrared solar absorption

701 measurements of XCO_2, XCH_4 and XCO at Xianghe, China. Earth System Science Data 12, 1679–1696.
702 https://doi.org/10.5194/essd-12-1679-2020

703 Zhang, G., Nan, Z., Hu, N., Yin, Z., Zhao, L., Cheng, G., Mu, C., 2022. Qinghai-Tibet Plateau Permafrost at Risk in
704 the Late 21st Century. Earth's Future 10, e2022EF002652. https://doi.org/10.1029/2022EF002652

705 Zhou, M., Ni, Q., Cai, Z., Langerock, B., Jiang, J., Che, K., Wang, J., Nan, W., Liu, Y., Wang, P., 2023. Ground-
706 Based Atmospheric CO2, CH4, and CO Column Measurements at Golmud in the Qinghai-Tibetan Plateau
707 and Comparisons with TROPOMI/S5P Satellite Observations. Adv. Atmos. Sci. 40, 223–234.
708 https://doi.org/10.1007/s00376-022-2116-0

709